Microscopic mechanisms behind the high mobility in rubrene single-crystal transistors as revealed by field-induced electron spin resonance

Kazuhiro Marumoto,[1,2,*] Norimichi Arai,[1] Hiromasa Goto,[1] Masashi Kijima,[1] Kouichi Murakami,[1] Yukihiro Tominari,[3] Jun Takeya,[2,3] Yukihiro Shimoi,[4] Hisaaki Tanaka,[5] Shin-ichi Kuroda,[5] Toshihiko Kaji,[6] Takao Nishikawa,[6] Taishi Takenobu,[2,6] and Yoshihiro Iwasa[7]

[1]*Institute of Materials Science, University of Tsukuba, Tsukuba 305-8573, Japan*
[2]*PRESTO, Japan Science and Technology Agency (JST), Kawaguchi 322-0012, Japan*
[3]*Graduate School of Science, Osaka University, Toyonaka 560-0043, Japan*
[4]*Nanosystem Research Institute (NRI), National Institute of Advanced Industrial Science and Technology (AIST), Tsukuba 305-8568, Japan*
[5]*Department of Applied Physics, Nagoya University, Nagoya 464-8603, Japan*
[6]*Institute for Materials Research, Tohoku University, Sendai 980-8577, Japan*
[7]*Quantum-Phase Electronics Center, The University of Tokyo, Tokyo 113-8656, Japan*

(Received 12 December 2010; published 4 February 2011)

The microscopic mechanisms behind the very high mobility in rubrene single-crystal transistors achieved by interface treatments with self-assembled monolayers (SAMs) have been clarified by using field-induced electron spin resonance (FI-ESR). Clearly observed FI-ESR signals exhibit extremely narrow linewidths owing to the very high carrier mobility. The precise angular dependence of FI-ESR g values shows that crystallinity in the semiconductor channel is unchanged by the SAM treatments. The trapping time of charge carriers at the interface directly evaluated from the ESR linewidth greatly decreases from ∼700 to ∼60 ps concomitant with the remarkable improvement in mobility because of the SAM treatments.

DOI: 10.1103/PhysRevB.83.075302 PACS number(s): 72.20.Jv, 76.30.−v, 81.05.Fb, 85.30.Tv

I. INTRODUCTION

Organic molecular devices (such as transistors, solar cells, and light-emitting diodes) have been investigated extensively because of their low cost, productivity, low environmental impact, and flexibility.[1–9] For organic field-effect transistors (FETs), it has been proven that the crystallinity of the channel semiconductor material plays a crucial role in improving the device's performance.[1–8] Single crystals of organic semiconductor molecules are quite effective at achieving high mobility in FETs.[3–8] Moreover, by use of a FET interface treatment with a self-assembled monolayer (SAM), rubrene single-crystal FETs (RSC-FETs) yielded the highest mobility of all organic FETs (40 $cm^2\ V^{-1}\ s^{-1}$), reaching two orders of magnitude higher than that of amorphous silicon.[9] The effects of the SAM interface treatment on the FET's characteristics have been studied by experimental and theoretical methods.[10–12] However, the mechanism behind the mobility improvement from the SAM interface treatment has not yet been fully clarified because the direct microscopic investigation of charge carriers, which are indispensable to higher mobility, is difficult. The conduction of carriers in RSC-FETs has been explained by a multiple trap and release (MTR) mechanism using the trapping time of charge carriers (τ_{tr}) at the FET interface.[7] Nevertheless, the τ_{tr} for RSC-FETs has not been directly determined so far.

Electron spin resonance (ESR) is a highly sensitive and powerful method that can be used to study organic materials at the molecular level.[13] We successfully investigated microscopic properties, such as the spin states, the spatial extent of charge carriers (the wave function of charge carriers), and the molecular orientation, of organic field-effect devices at the FET interface by field-induced electron spin resonance (FI-ESR).[14–16] This FI-ESR method has also been developed by other groups.[17,18] The FI-ESR method, however, has mainly been applied to thin film devices with low mobility, below 0.6 $cm^2\ V^{-1}\ s^{-1}$, using pentacene and regioregular poly(3-alkylthiopene).[14–18] The microscopic mechanism behind high mobility, above 1 $cm^2\ V^{-1}\ s^{-1}$, has not been investigated by FI-ESR previously to our knowledge.

In this paper, we utilize the FI-ESR technique as a probe for investigating the microscopic mechanism behind very high mobility by excluding extrinsic effects, such as contact resistance. We report a direct determination of the τ_{tr} for RSC-FETs. We fabricated RSC-FETs with different kinds of SAM interface treatment. These devices show good FET performance and very clear FI-ESR signals. We demonstrate that the ESR linewidth, which reflects the local dynamics of charge carriers in the FET channel, is clearly correlated with the field-effect mobility. The evaluated τ_{tr} greatly decreased from ∼700 to ∼60 ps concomitant with the remarkable increase in the mobility after the SAM interface treatment. Another piece of important information obtained from the ESR analysis concerns the molecular orientations at the FET interfaces. The anisotropy of the ESR signal can be explained by the same molecular orientation found in bulk crystals. Therefore, we microscopically discovered that the SAM interface treatment greatly decreases τ_{tr} without a significant change in the semiconductor channel's crystallinity.

II. DEVICE FABRICATION

Figure 1(a) illustrates the schematic structure of the RSC-FETs that were used in our ESR measurements. The RSCs were grown by physical vapor transport.[8,9] Typical crystal dimensions were 0.5 mm × 2 mm × 1 μm. The dimensions of the SiO_2/Si substrate were 3 × 30 mm^2. A 300 nm layer

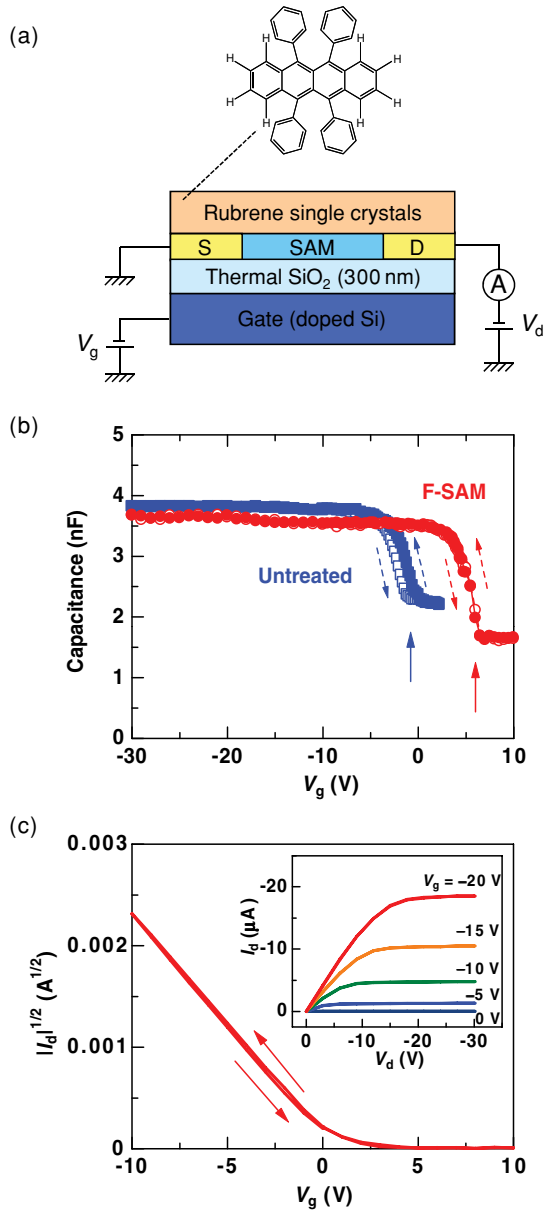

FIG. 1. (Color online) (a) Schematic structure of an RSC-FET with the SAM interface treatment. (b) V_g dependence of the capacitance of RSC-FETs with the F-SAM interface treatment (circles) and without the interface treatment (squares). (c) Transfer characteristics of the untreated FET. Inset: Output characteristics of the same device.

of thermally grown SiO_2 served as a gate dielectric with a capacitance of 11.9 nF/cm^2. Source-drain electrodes of Cr (3 nm)/Au (17 nm) were vapor deposited through a shadow mask. The channel length L was 0.25–0.85 mm and the channel width W was 12–22 mm (W/L = 18–86) depending on the device. Twenty or more thin crystals were attached to the substrate electrostatically with the same crystal axis orientation. Our FETs for ESR measurements feature long channel lengths ($L \geqslant 0.25$ mm) (see Table I). The FETs were fabricated by laminating organic crystals against a silicon wafer with predeposited electrodes.[8,9] This method eliminates the need to deposit metals and dielectrics directly onto a very fragile organic surface.[5] This technique, in combination with

TABLE I. Field-effect mobility μ, peak-to-peak ESR linewidth ΔH_{pp}, trapping time of the charge carriers τ_{tr}, and channel length L for RSC-FETs with an interface treatment of SAM or PMMA, and without an interface treatment.

Interface treatment	μ (cm^2 V^{-1} s^{-1})	ΔH_{pp} (G)	τ_{tr} (ps)	L (mm)
F-SAM	7.68	0.070 ± 0.007	60 ± 40	0.31
CH_3-SAM	3.52	0.080 ± 0.008	230 ± 60	0.25
PMMA	0.53	0.105 ± 0.010	630 ± 100	0.79
Untreated	1.20	0.105 ± 0.010	630 ± 100	0.36
Untreated	0.72	0.110 ± 0.010	710 ± 100	0.85

interface treatments of perfluorotriethoxysilane (F-SAM) or decyltriethoxysilane (CH_3-SAM),[10] yields the highest field-effect mobility of all organic FETs.[9] We utilized the same SAM materials in this work. The SAM was formed by dry chemical vapor deposition so that a monolayer selectively covered the SiO_2.[10] For comparison, the FET interface was also treated with poly(methyl methacrylate) (PMMA); a PMMA thin film was spin coated on the SiO_2 surface. The present FET structure is known as a bottom-contact configuration; previous devices that were used for ESR measurements had a top-contact configuration.[14–18]

III. RESULTS AND DISCUSSION

A. Operation of RSC-FETs

We present first the operation of the RSC-FETs. Figure 1(b) shows the dependence of the capacitance (C) on the gate voltage (V_g) for the FET with an F-SAM interface treatment (F-SAM FET) and without an interface treatment (untreated FET). The capacitance characteristics were measured with a Hioki 3511-50 *LCR* meter with a modulation frequency of 120 Hz at 290 K. For both devices, C sharply increased with $|V_g|$ for $V_g < 0$ and then plateaued at 3.7–3.8 nF from the accumulation of hole carriers at the FET interface. The threshold voltage (V_{th}^C) for the sharp increase in C clearly shifts to positive values from $V_{th}^C \sim -1$ V (the untreated FET) to $V_{th}^C \sim 6$ V (the FET with the F-SAM interface treatment). The V_{th}^C of the FETs with the PMMA and CH_3-SAM interface treatment (PMMA FET and CH_3-SAM FET) were evaluated as $\sim$0 and $\sim$5 V, respectively. These positive shifts for SAM FETs are consistent with those for pentacene FETs,[10] indicating that the SAM interface treatment works well in our devices.

Figure 1(c) shows the transfer characteristics of the untreated FET. The FET characteristics were measured by using a Keithley 4200-SCS semiconductor parameter analyzer at 290 K. A steep increase in the drain current I_d for $V_g < 0$ was observed. The inset of Fig. 1(c) shows the output characteristics of the same FET. Very clear saturation behavior is observed at high drain voltages V_d. Similar FET characteristics were confirmed for all other FETs. These characteristics demonstrate that our FETs show standard, good p-type semiconductor FET operation. The fact that almost no hysteresis behavior was observed in the capacitance and FET characteristics probably indicates that there are almost no deep traps in the induced charge or migration of low-mobility dopant ions toward the accumulation layer.[19] This is probably due

to the very clean and well-defined FET interface that arises from lamination of purified single crystals.[8,9] We evaluated the field-effect mobility μ by using a two-point probe in the saturation regime, using the formula $I_d = (W/2L)\mu C_{SiO_2}(V_g - V_{th})^2$, with the capacitance C_{SiO_2} of the SiO_2 insulator and the threshold voltage V_{th}. The evaluated μ is summarized in Fig. 4 and Table I. Note that one F-SAM FET exhibits the highest mobility (7.68 $cm^2\ V^{-1}\ s^{-1}$) of all the organic FETs used for ESR measurements. The device dependence for the mobility is 20%–40%. The devices were sealed into ESR sample tubes under vacuum conditions. The lifetime of the device with highest mobility was confirmed to be at least one year.

B. FI-ESR signals of RSC-FETs

We next present the FI-ESR signals of the RSC-FETs. The FI-ESR signal was obtained by subtracting the signal at $V_g > 0$ under depletion conditions from that at $V_g < 0$ to account for hole-carrier accumulation. Figures 2(a) and 2(b) show ESR signals for the untreated FET and F-SAM FET at 290 K, respectively. The solid and dashed lines show the data at $V_g < 0$ and $V_g > 0$, respectively. The ESR measurements were performed with a JES-FA200 *X*-band spectrometer. The *g* value and ESR intensity were calibrated using a standard-maker sample of Mn^{2+}. For the capacitance and ESR measurements, the source and drain electrodes were also short-circuited and grounded, forming a metal-insulator-semiconductor (MIS) diode structure with no lateral applied field between these electrodes. At $V_g > 0$, no ESR signal was observed from rubrene, which is consistent with the fact that undoped rubrene has no ESR signal.[1] In sharp contrast, we successfully observed clear FI-ESR signals at $V_g = -30$ V. Both of the *g* values were evaluated as $2.002\ 40 \pm 0.000\ 05$, which is ascribed to the π electrons of rubrene. The line shape of the FI-ESR signal is Lorentzian. The observed peak-to-peak ESR linewidth (ΔH_{pp}) was below 0.11 G, which is much narrower than that for organic thin film devices.[14–18] This result can be ascribed to motional narrowing due to very-high-mobility carrier motion. A similar, extremely narrow linewidth was also observed for the CH_3-SAM FET and PMMA FET. The evaluated values of ΔH_{pp} are summarized in Fig. 4 and Table I.

We evaluated the number of field-induced spins N_{spin} from the FI-ESR signals at various V_g. N_{spin} was obtained by twice integrating the first derivative of the ESR signal, assuming the Curie law. The inset in Fig. 2(a) shows the dependence of N_{spin} on V_g (solid circles) for the untreated FET. The number of field-induced charge carriers, N_{charge} (open squares), was evaluated from $Q = C_{rubrene}|V_g - V_{th}|$, where Q is the charge and $C_{rubrene}$ is the capacitance due to rubrene for the whole active area. N_{spin} and N_{charge} linearly increased as $|V_g|$ increased and reached 3.3×10^{11} (with a density of 2.8×10^{12} cm^{-2}) and 3.4×10^{11} (2.9×10^{12} cm^{-2}), respectively, at $V_g = -30$ V. The spin concentration was calculated to be ~1% per molecular unit at $V_g = -30$ V, which takes into consideration the RSC lattice constants. N_{spin} is excellently proportional to N_{charge}, which definitively demonstrates that all of the field-injected carriers have $S = 1/2$ spins. Note that the carriers observed by FI-ESR are the same carrier species as those observed moving in the FET channels. The present MIS diodes show good FET operation when a drain voltage is applied between the source and drain electrodes, as shown in Fig. 1(c). Similar results were confirmed for all of the other FETs.

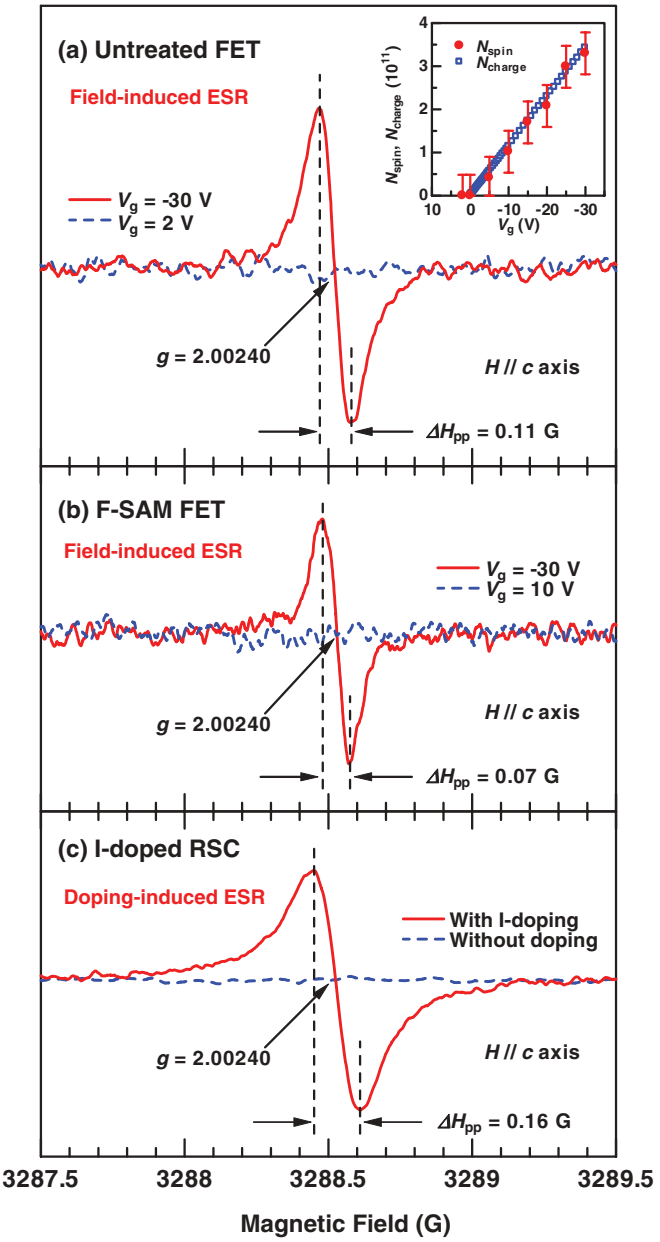

FIG. 2. (Color online) (a) FI-ESR signal of the untreated FET. Inset: V_g dependence on N_{spin} (solid circles) and N_{charge} (open squares) at 290 K. (b) FI-ESR signal of the F-SAM FET. (c) DI-ESR signal of RSCs at 290 K. The solid and dashed lines show the data with and without doping, respectively.

C. Anisotropy of FI-ESR signals

We next present the anisotropy of the FI-ESR signal's *g* values, which microscopically clarifies the molecular orientation of RSCs at the FET interfaces. Figures 3(a) and 3(b) show data for an external magnetic field *H* in the *b*-*c* and *a*-*c* planes of the crystal. Here, Θ is defined as the angle between *H* and the *c* axis of the RSCs. All of the data with different interface treatments

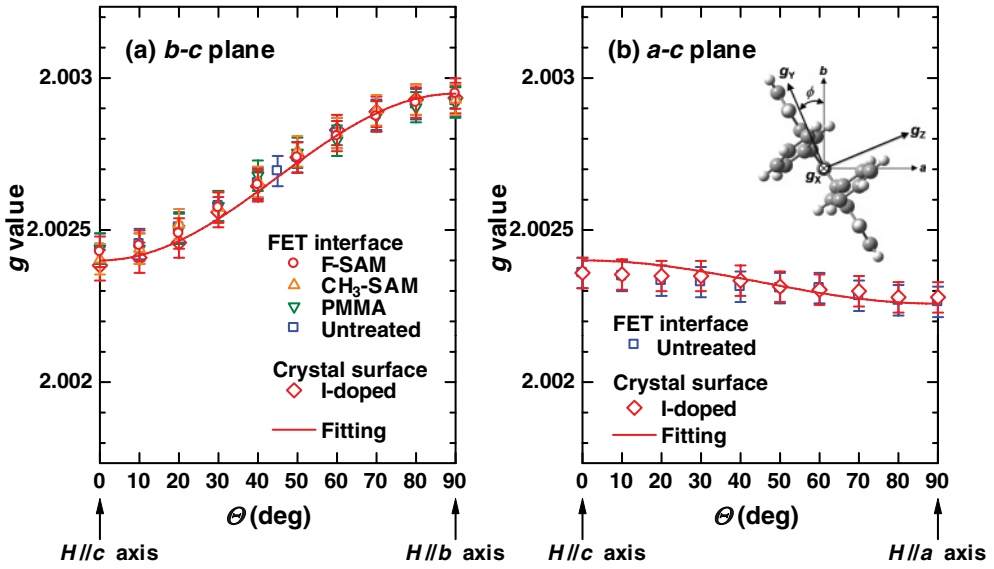

FIG. 3. (Color online) Anisotropic ESR g values at 290 K for H in the b-c plane (a) and in the a-c plane (b): F-SAM FET (circles), CH_3-SAM FET (up triangles), PMMA FET (down triangles), untreated FET (squares), and iodine-doped RSC (diamonds). The FI-ESR signals were measured at $V_g = -30$ V. The solid lines show fitted curves. Inset: The principal axes of the g tensor calculated by a DFT calculation for an isolated rubrene molecule.

coincide with each other within experimental error, which demonstrates that the molecular orientation at the interface does not depend on interface treatment, whether it be F-SAM, CH_3-SAM, or PMMA. We confirmed this anisotropic feature in doping-induced ESR (DI-ESR) measurements and by using iodine as the dopant [see Figs. 2(c) and 3, and Appendix A].

The observed anisotropy of the g values can be explained using the molecular structure in the crystal. The principal axis of the g tensor is defined in the inset of Fig. 3(b). Owing to the C_{2h} symmetry of the crystal's molecular structure, the direction of g_x coincides with the c axis, while those of g_y and g_z are in the a-b plane. ϕ is defined as the angle between the direction of g_y and the b axis. When the applied magnetic field H is within the a-c plane, the g value is expressed as $g(\Theta) = g_e + \Delta g_x \cos^2\Theta + \Delta g_y \sin^2\phi \sin^2\Theta + \Delta g_z \cos^2\phi \sin^2\Theta$. Here, $g_e = 2.002\,319\,3$ is the g value of a free electron and Δg_i is the g shift in the i direction. In the b-c plane, the terms $\sin^2\phi$ and $\cos^2\phi$ are exchanged in this formula. The solid lines in Fig. 3 are fitted curves that used these expressions. The fitting was carried out against the data for the untreated FET, where g_x, g_y, and g_z are employed as the fitting parameters, while ϕ is fixed to a value determined by a density functional theory (DFT) calculation (22.96°) for an isolated rubrene molecule. The fitting reproduces the observed data quite well. The g shifts obtained by the fitting are $\Delta g_x = 81$, $\Delta g_y = 780$, and $\Delta g_z = -213$ ppm. Therefore, the molecular orientation at the FET interface can be understood from an FI-ESR investigation in combination with a theoretical analysis. The molecular g tensor calculated by the DFT method is described in Appendix B.

D. Correlation between FET and ESR characteristics

Finally, we demonstrate that the FET and ESR characteristics have a clear correlation with each other. As shown in Fig. 4 and Table I, μ remarkably improved with the SAM interface treatment, and ΔH_{pp} significantly decreased. This correlation can be ascribed to a large decrease in τ_{tr} at the FET interface, which largely determines the mobility and ESR linewidth as described below. Generally speaking, spin-spin relaxation and spin-lattice relaxation contribute to the ESR linewidth.[20] According to motional narrowing theory,[21] the former contribution is proportional to a spin-correlation time, which is nothing but τ_{tr}. Thus, when a Lorentzian linewidth is extremely narrow, it can be expressed as follows:

$$\frac{\sqrt{3}}{2}\Delta H_{pp} = \gamma\,(\Delta H_d)^2\,\tau_{tr} + \frac{1}{2\gamma T_1}. \qquad (1)$$

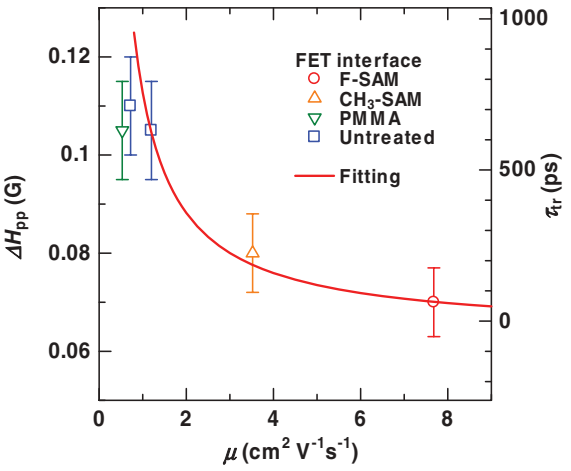

FIG. 4. (Color online) Correlation between peak-to-peak ESR linewidth ΔH_{pp} and the field-effect mobility μ at 290 K. The solid line is a fitted curve using Eq. (3). The ordinate on the right-hand side is the trapping time τ_{tr} of the charge carriers defined in Eq. (1).

Here, ΔH_d is the static linewidth that arises from hyperfine interactions between carrier spins and hydrogen nuclear spins. ΔH_d was precisely evaluated to be 1.74 G from the half width at half maximum of the absorption peak of the DI-ESR for RCSs at 4 K, where the motional narrowing effect is negligible. The second term is the spin-lattice-relaxation linewidth that is determined by the spin-lattice-relaxation time (T_1). γ is the gyromagnetic ratio for rubrene π electrons. By using the value of $T_1 = 0.5\ \mu$s, which was determined by the continuous-wave saturation method in the ESR measurements,[22] we can directly evaluate τ_{tr} from Eq. (1). As shown in Fig. 4 and Table I, τ_{tr} greatly decreased from ~700 to ~60 ps when the mobility remarkably increased from ~1 to ~8 $cm^2\ V^{-1}\ s^{-1}$ after the SAM interface treatment. The magnitude of τ_{tr} is of the same order as the value determined from the photoinduced charge density in tetracene single-crystal FETs.[4]

For further discussion of the correlation between the ESR linewidth and the mobility, we tried to adopt the conventional MTR model.[4,7] In this model, carriers diffusively move with an intrinsic mobility μ_0 between trapping events. The observed mobility μ is reduced by trapping:

$$\mu = \mu_0 \frac{\tau}{\tau + \tau_{tr}}. \tag{2}$$

Here, τ is the average time of diffusive motion between trapping events. By combining Eq. (1) with Eq. (2), ΔH_{pp} is expressed as a function of μ:

$$\frac{\sqrt{3}}{2}\Delta H_{pp} = \gamma\,(\Delta H_d)^2 \left(\frac{\mu_0}{\mu} - 1\right)\tau + \frac{1}{2\gamma T_1}. \tag{3}$$

Under the simple assumption that τ is identical for all the samples, we analyze the correlation between ΔH_{pp} and μ using Eq. (3). The fitting curve shown in Fig. 4 explains the overall behavior of the observed correlation. The product $\mu_0\tau$ was determined to be $7.96 \times 10^{-10}\ cm^2\ V^{-1}$.

As shown in Fig. 3, the molecular orientation at the FET interface does not depend on the interface treatment. This is in sharp contrast to crystallinity changes that are often pointed out in thin film FETs.[10,23] Nevertheless, only the SAM interface treatment has the effect of decreasing τ_{tr}. The PMMA interface treatment does not decrease τ_{tr}. A probable explanation for the above difference is that it is due to different interactions at FET interfaces between RSCs and SAM or PMMA: the SAM interface is very clean owing to periodic self-assembling molecular alignment, while the PMMA interface must be random because of its polymeric nature. These different interactions might lead to different trapping states for charge carriers. Although the detailed origin of τ_{tr} is still open for further studies, we microscopically detected at least that the SAM interface treatment greatly decreases τ_{tr} at the FET interface. Such an effect is clearly found only by using single-crystal FETs with very high mobility. Actually, the recent improvement in FET performance has mainly been achieved by improving molecular crystallinity. Hence, the SAM interface treatment is extremely effective in further improving the performance of organic FETs with high crystallinity.

IV. SUMMARY

We presented an effective method for investigating the microscopic mechanism behind the very high mobility in rubrene single-crystal FETs by using the FI-ESR technique, which excludes extrinsic effects such as contact resistance and grain boundaries. The mechanism of very high mobility has been successfully clarified from a microscopic viewpoint by directly evaluating the trapping time of charge carriers (τ_{tr}) at the FET interface from the observed FI-ESR signal. The SAM interface treatment greatly decreased τ_{tr}, without changing the interface molecular crystallinity, which resulted in a remarkable improvement in mobility. Microscopic probes such as ESR, which have not been popular in organic transistors, are extremely useful for elucidating intrinsic transport mechanisms in high-mobility organic devices. The present result indicates that interface design should play a key role in further improvements to highly crystalline organic transistors for next generation devices.

ACKNOWLEDGMENTS

This work was supported by Grants-in-Aid for Scientific Research (No. 21560008 and No. 22340080) from the JSPS of Japan, and by the JST PRESTO program.

APPENDIX A: DOPING-INDUCED ESR OF RSCs

Samples of iodine-doped RSCs were fabricated by laminating thin crystals on a substrate of poly(ethylene terephthalate), which were then doped with iodine vapor at a very low concentration. Figure 2(c) shows an observed doping-induced ESR signal from such a sample. The DI-ESR intensity increased with doping times above 3 s and showed a tendency to saturation, while the g value and narrow ΔH_{pp} do not depend on the doping time up to 60 min. These results probably indicate that iodine ions are adsorbed only at the surface of RSCs, otherwise the g and ΔH_{pp} values would strongly depend on the doping time and show larger g ($g = 2.006$) and ΔH_{pp} ($\Delta H_{pp} = 11.5$ G) values due to the intercalations of iodine ions, as was reported for heavily iodine-doped RSCs.[24] As shown in Fig. 3 the anisotropy of the g value for the iodine-doped RSCs is consistent with that of the FET interface.

APPENDIX B: MOLECULAR g TENSOR OF RUBRENE CALCULATED BY DFT METHOD

The g tensor's orthorhombicity was discussed in Sec. III C. This feature was also confirmed from a DFT calculation. A DFT calculation of the g tensor for an isolated rubrene molecule was carried out with the B3LYP functional and 6-31G(d) basis set by using the gaussian 03 software package.[25] The molecular geometry was taken from the crystal structure, which was determined at room temperature.[26,27] Note that, in this paper, the a and c crystal axes are exchanged as compared to Ref. 27. The g tensor was computed for a cationic state by using the gauge-independent atomic orbital method. The calculated principal values are $\Delta g_x = 171$, $\Delta g_y = 699$, and $\Delta g_z = 10$ ppm. These values are consistent with those obtained by fitting and both results show a similar anisotropic feature, although the calculated g

values are somewhat dependent on the functionals employed. The calculated value of ϕ (the angle between the direction of g_y and the b axis) is 22.96°, which implies that the principal axes in the a-b plane are tilted slightly from the molecular axis by approximately 8° [see the inset of Fig. 3(b)].

*Corresponding author; marumoto@ims.tsukuba.ac.jp.

[1]M. F. Calhoun, J. Sanchez, D. Olaya, M. E. Gershenson, and A. V. Podzorov, Nature Mater. **7**, 84 (2008).
[2]Y. Zhou, T. Lei, L. Wang, J. Pei, Y. Cao, and J. Wang, Adv. Mater. **22**, 1484 (2010).
[3]O. D. Jurchescu, M. Popinciuc, B. J. van Wees, and T. T. M. Palstra, Adv. Mater. **19**, 688 (2007).
[4]M. F. Calhoun, C. Hsieh, and V. Podzorov, Phys. Rev. Lett. **98**, 096402 (2007).
[5]V. C. Sunder, J. Zaumseil, V. Podzorov, E. Menard, R. L. Willett, T. Someya, M. E. Gershenson, and J. A. Rogers, Science **303**, 1644 (2004).
[6]E. Menard, V. Podzorov, S.-H. Hur, A. Gaur, M. E. Gershenson, and J. A. Rogers, Adv. Mater. **16**, 2097 (2004).
[7]V. Podzorov, E. Menard, J. A. Rogers, and M. E. Gershenson, Phys. Rev. Lett. **95**, 226601 (2005).
[8]J. Takeya, J. Kato, K. Hara, M. Yamagishi, R. Hirahara, K. Yamada, Y. Nakazawa, S. Ikehata, K. Tsukagoshi, Y. Aoyagi, T. Takenobu, and Y. Iwasa, Phys. Rev. Lett. **98**, 196804 (2007).
[9]J. Takeya, M. Yamagishi, Y. Tominari, R. Hirahara, Y. Nakazawa, T. Nishikawa, T. Kawase, T. Shimoda, and S. Ogawa, Appl. Phys. Lett. **90**, 102120 (2007).
[10]S. Kobayasi, T. Nishikawa, T. Takenobu, S. Mori, T. Shimoda, T. Mitani, H. Shimotani, N. Yoshimoto, S. Ogawa, and Y. Iwasa, Nature Mater. **3**, 317 (2004).
[11]P. Pacher, A. Lex, P. Proschek, H. Etschmaier, E. Tchernychova, M. Sezen, U. Scherf, W. Grogger, G. Trimmel, C. Slugovc, and E. Zojer, Adv. Mater. **20**, 3143 (2008).
[12]S. K. Possanner, K. Zojer, P. Pacher, E. Zojer, and F. Schürrer, Adv. Funct. Mater. **19**, 958 (2009).
[13]K. Marumoto, M. Kato, H. Kondo, S. Kuroda, N. C. Greenham, R. H. Friend, Y. Shimoi, and S. Abe, Phys. Rev. B **79**, 245204 (2009).
[14]K. Marumoto, Y. Muramatsu, Y. Nagano, T. Iwata, S. Ukai, H. Ito, S. Kuroda, Y. Shimoi, and S. Abe, J. Phys. Soc. Jpn. **74**, 3066 (2005).
[15]K. Marumoto, S. Kuroda, T. Takenobu, and Y. Iwasa, Phys. Rev. Lett. **97**, 256603 (2006).
[16]H. Tanaka, S. Watanabe, H. Ito, K. Marumoto, and S. Kuroda, Appl. Phys. Lett. **94**, 103308 (2009).
[17]H. Matsui, T. Hasegawa, Y. Tokura, M. Hiraoka, and T. Yamada, Phys. Rev. Lett. **100**, 126601 (2008).
[18]H. Matsui, A. S. Mishchenko, and T. Hasegawa, Phys. Rev. Lett. **104**, 056602 (2010).
[19]P. J. Brown, H. Sirringhaus, M. Harrison, M. Shkunov, and R. H. Friend, Phys. Rev. B **63**, 125204 (2001).
[20]N. Bloembergen, *Nuclear Magnetic Relaxation* (W. A. Benjamin, New York, 1961).
[21]R. Kubo and K. Tomita, J. Phys. Soc. Jpn. **9**, 888 (1954).
[22]R. S. Alger, *Electron Paramagnetic Resonance: Techniques and Applications* (John Wiley & Sons, New York, 1968).
[23]D. J. Gundlach, J. A. Nichols, L. Zhou, and T. N. Jackson, Appl. Phys. Lett. **80**, 2925 (2002).
[24]M. Kameya, T. Naito, and T. Inabe, Bull. Chem. Soc. Jpn. **73**, 61 (2000).
[25]M. J. Frisch *et al.*, computer code GAUSSIAN 03, Revision C.02 (Gaussian, Inc., Wallingford, CT, 2004).
[26]F. H. Allen, Acta Crystallogr. B **58**, 380 (2002).
[27]O. D. Jurchescu, A. Meetsma, and T. T. M. Palstra, Acta Crystallogr. B **62**, 330 (2006).